

A General Method for Multimetallic Platinum Alloy Nanowires as Highly Active and Stable Oxygen Reduction Catalysts

Lingzheng Bu, Jiabao Ding, Shaojun Guo,* Xu Zhang, Dong Su, Xing Zhu, Jianlin Yao, Jun Guo, Gang Lu, and Xiaoqing Huang*

The production of inorganic nanoparticles (NPs) with precise control over structures has always been a central target in various fields of chemistry and physics because the properties of NPs can be desirably manipulated by their structure.^[1–4] There has been an intense search for high-performance noble metal NP catalysts particular for Pt.^[5–9] Precious platinum (Pt) NPs are active catalysts for various heterogeneous reactions and show particularly superior performance in both the anodic oxidation reaction and the cathodic oxygen reduction reaction (ORR) in the fuel cells, but their rare content and high cost largely impede the practical application.^[10–12] A potential strategy to address this tremendous challenge is alloying Pt NPs with the transition metals (TMs).^[13–16] Because of the well-tuned electronic properties of Pt by TM and the improved number of accessible Pt sites in the alloy, the Pt alloy NPs can exhibit much enhanced performance for ORR compared with monometallic Pt counterpart despite its reduced content of scarce Pt.^[16,17] Extensive research efforts have been devoted to controlling Pt alloy NPs in a wide range of shapes, structures, and compositions.^[18–32] The well-defined Pt alloy NPs prepared so far are mainly dominated by shapes such as sphere, cube,

octahedron, and tetrahedron.^[18–32] Unfortunately, those conventional Pt alloy multimetallic NPs have big limitations in terms of catalytic durability and thermal stability. They undergo structural transformation quickly under detrimental corrosive catalytic conditions or in high-temperature catalytic process, resulting in undesirable performance loss.^[20,33,34]

Considering the superior properties of 1D nanostructure, such as inherent anisotropic morphology, high flexibility, high surface area, and high conductivity, one would expect 1D Pt alloy nanostructure to be an ideal structure for improving both the utilization efficiency of Pt and the stability of the catalysts.^[35,36] However, the major limitation of previous synthetic methods exploiting 1D Pt alloy nanostructures for efficient catalysis is largely limited by the lack of a robust method that enables the general preparation of 1D Pt alloy multimetallic nanostructures with desired composition. Another important strategy to enhance the catalysis is to customize the metal NPs with high-index crystallographic facets.^[37] The atoms located at steps, ledges, and kinks of high-indexed nanocrystals can act as additional catalytically active sites, and are significant to rationally design and prepare shape-controlled nanocatalysts with high density of low-coordinated atoms for enhanced catalysis.^[37] In this regard, the rational introduction of high-index facets into 1D Pt-based nanostructure may provide a promising approach to maximize the utilization of Pt for achieving very high ORR activity and stability, but it is still a great challenge.

Herein, we, for the first time, report a robust and general wet-chemical route that enables the large-scalable production of multimetallic Pt-based 1D nanostructures with high density of low-coordinate atomic steps for multiple catalysis enhancement, which can well address several major design criteria for advanced nanoscale electrocatalysts, namely, high surface-to-volume ratio, alloy effect, 1D morphology, and high-index facet. Several important features of our synthetic approach to this new class of 1D Pt alloy nanostructures can be highlighted: (1) a broad range of compositions for these 1D Pt alloys, from bimetallic to trimetallic nanowires, is produced at high yield by a simple, general, and large-scalable wet-chemical route. (2) The unique 1D structural feature combined with the alloying effects enhances the catalytic properties of the produced Pt alloy nanostructures. (3) These 1D Pt alloy nanostructures have a high density of atomic steps, ledges, and kinks, serving as an additional yet very important role in enhancing catalysis. As a demonstration, we found that these unique high-index faceted 1D PtNi nanostructures exhibit high ORR catalytic performance with an excellent specific activity of 9.2 mA cm⁻² and a

L. Bu, J. Ding, Prof. J. Yao, Prof. X. Huang
College of Chemistry
Chemical Engineering and Materials Science
Soochow University
Jiangsu 215123, China
E-mail: hxq006@suda.edu.cn



Prof. S. Guo
Department of Materials Science and Engineering
and Department of Energy and Resources Engineering
College of Engineering
Peking University
Beijing 100871, P. R. China
E-mail: sjguo@coe.pku.edu.cn

Dr. X. Zhang, Prof. G. Lu
Department of Physics and Astronomy
California State University
Northridge, CA 91330, USA

Dr. D. Su
Center for Functional Nanomaterials
Brookhaven National Laboratory
Upton, NY 11973, USA

Dr. X. Zhu, Prof. J. Guo
Testing and Analysis Center
Soochow University
Jiangsu 215123, China

DOI: 10.1002/adma.201502725

very high mass activity of $4.15 \text{ A mg}_{\text{Pt}}^{-1}$ at 0.9 V versus reversible hydrogen electrode (RHE), which are 51.1 times and 34.6 times higher than those of the state-of-the-art commercial Pt/C catalyst (Johnson Matthey (JM), 20 wt% Pt, 0.18 mA cm^{-2} and $0.12 \text{ A mg}_{\text{Pt}}^{-1}$), making the as-prepared 1D PtNi catalyst among the most active electrocatalyst for ORR reported to date. (4) Significantly, the obtained 1D PtNi nanostructures are highly stable in the ORR condition with negligible activity decay over the course of 10 000 cycles. Computational studies indicate the extremely high ORR activity on the 1D PtNi catalyst should be caused by optimal oxygen adsorption energy (E_{O}) at the hollow sites on the (211) and (311) high-index facets of nanowires (NWs). These results demonstrate that these new classes of 1D high-index faceted Pt alloy nanostructures produced by our new method reported herein are promising material candidates with much enhanced performance for practical catalytic applications.

The unique 1D Pt alloy nanostructures were produced by simultaneous reduction of platinum(II) acetylacetonate ($\text{Pt}(\text{acac})_2$) and a desired acetylacetonate compound ($\text{M}(\text{acac})_x$, such as $\text{Ni}(\text{acac})_2$, $\text{Co}(\text{acac})_3$, $\text{Fe}(\text{acac})_3$, $\text{Rh}(\text{acac})_3$, or the combination of them) by the use of oleylamine as solvent and surfactant, cetyl trimethylammonium chloride (CTAC) as the structure-directing agent, and glucose as a

reducing agent. In a typical synthesis, $\text{Pt}(\text{acac})_2$, $\text{M}(\text{acac})_x$, glucose, CTAC, and oleylamine were added into a vial (see the Supporting Information for details). After the glass vial had been capped, the mixture was ultrasonicated for around 1 h. The resulting homogeneous mixture was then heated at room temperature to $200 \text{ }^\circ\text{C}$ (or $210 \text{ }^\circ\text{C}$) and kept at $200 \text{ }^\circ\text{C}$ (or $210 \text{ }^\circ\text{C}$) for 5 h in an oil bath, before it was cooled to room temperature. The resulting black colloidal products were collected by centrifugation and washed three times with an ethanol/cyclohexane mixture.

The morphology and structure of the resulting 1D high-index faceted Pt alloy nanostructures were characterized by transmission electron microscopy (TEM) and high-angle annular dark-field scanning TEM (HAADF-STEM). Using PtNi as an example, it is found that abundant 1D nanostructure was the dominant product with the yield approaching 100% (Figure 1a,b and Figure S1, Supporting Information). It exhibits high aspect ratio with the length of hundreds of nanometers and the diameter of around 9 nm (Figure 1c–e and Figure S1, Supporting Information). These PtNi nanowires are frequently bent on the TEM grid, indicating that they are highly flexible (Figure 1e and Figure S1, Supporting Information). It should be noticed that all the surveyed nanowires have an uneven

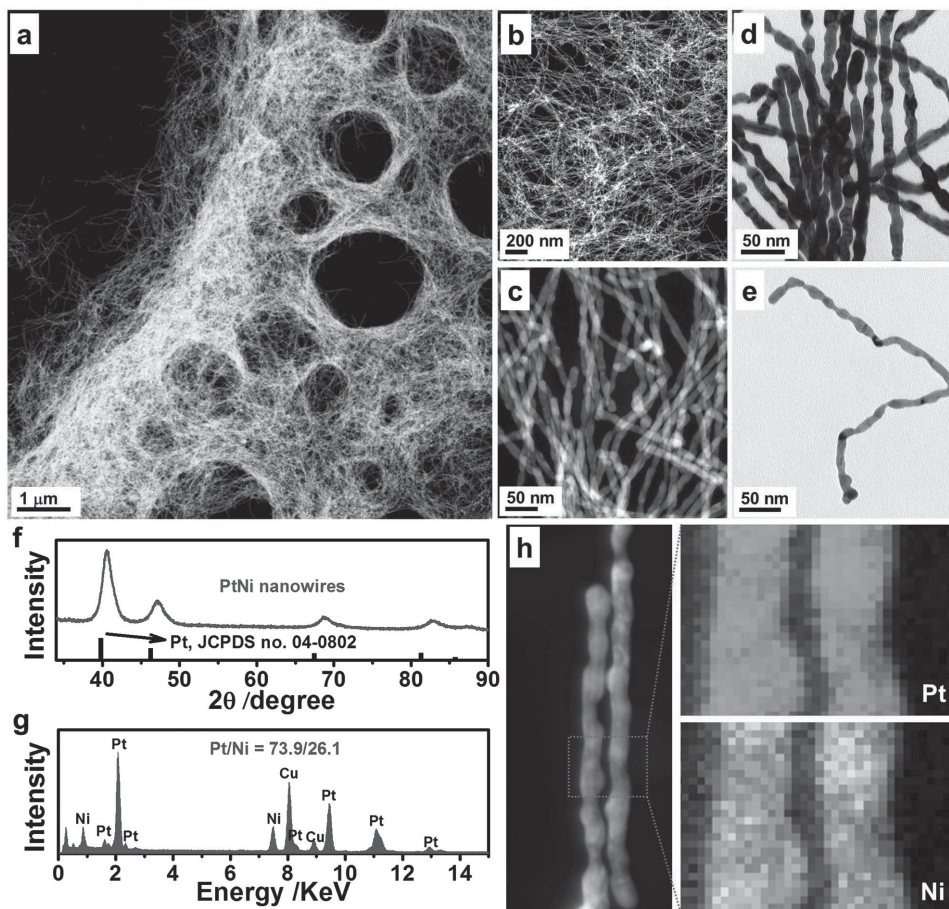


Figure 1. Morphology and structure characterizations of 1D PtNi nanostructures. Representative a–c) STEM images, d,e) TEM images, f) PXRD pattern, g) EDS spectrum, and h) STEM-ADF image and EDS elemental mapping of the 1D PtNi nanostructures. The composition is $\text{Pt}/\text{Ni} = 74.2 \pm 0.3/25.8 \pm 0.3$, as confirmed by ICP-AES. The composition is $\text{Pt}/\text{Ni} = 73.9 \pm 0.5/26.1 \pm 0.5$, as confirmed by TEM-EDS.

ultrathin diameter along their entire length (Figure 1c–e and Figure S1, Supporting Information). Those unusual features of 1D PtNi nanostructures reported here suggest that a unique mechanism might dominate their growth. The microstructure of 1D PtNi nanostructures was further characterized by powder X-ray diffraction (PXRD) (Figure 1f). The PXRD pattern of the products displays the distinct face-center-cubic (fcc) pattern associated with Pt₃Ni, being in agreement with that of the previous report.^[38] The Pt/Ni composition is $74.2 \pm 0.3/25.8 \pm 0.3$, as confirmed by inductively coupled plasma atomic emission spectroscopy (ICP-AES) and TEM energy-dispersive X-ray spectroscopy (TEM-EDS, $73.9 \pm 0.5/26.1 \pm 0.5$) (Figure 1g). The alloyed nanostructure was confirmed by the STEM-EDS elemental mapping analysis, where the distribution of Pt and Ni is high even through the analyzed area (Figure 1h).

The crystalline nature of the obtained 1D PtNi nanostructures was initially analyzed by high-resolution TEM (HRTEM) measurement. As shown in Figure 2a, the majority of displayed facet shows lattice fringes with an interplanar spacing of 0.19 nm, corresponding to the (200) plane of fcc Pt₃Ni alloy nanostructure. The atomic structure of the 1D PtNi nanostructures was

further characterized by the aberration-corrected HRTEM and STEM. These characterizations provide atomic-resolution images of the outmost layer of nanostructures, which are important in identifying surface structures. Two aberration-corrected images from the same 1D PtNi nanostructure are shown in Figure 2b,c, in which the border atoms are clearly resolved. The crystal orientation of the structure is along the zone axis of $\langle 110 \rangle$. The surface of the 1D PtNi nanostructure is not smooth, as many small facets can be clearly observed. Characteristically, a high density of low-coordinate atomic steps, such as {211}, and {311} steps, was frequently observed around the surface of the 1D PtNi nanostructure (Figure 2b,c and Figures S2–S3, Supporting Information). The presence of high density of low-coordinate atomic steps can promote oxygen adsorption, and thus is beneficial for ORR.^[37]

There are several important reaction parameters that impact the production of high-quality 1D PtNi alloy nanostructures. (1) The use of CTAC was the major factor in producing 1D PtNi alloy nanostructures. As shown in Figure S4a,b (Supporting Information), the reaction in the absence of CTAC could just yield the branched nanocrystals with a size of 37 ± 5 nm.

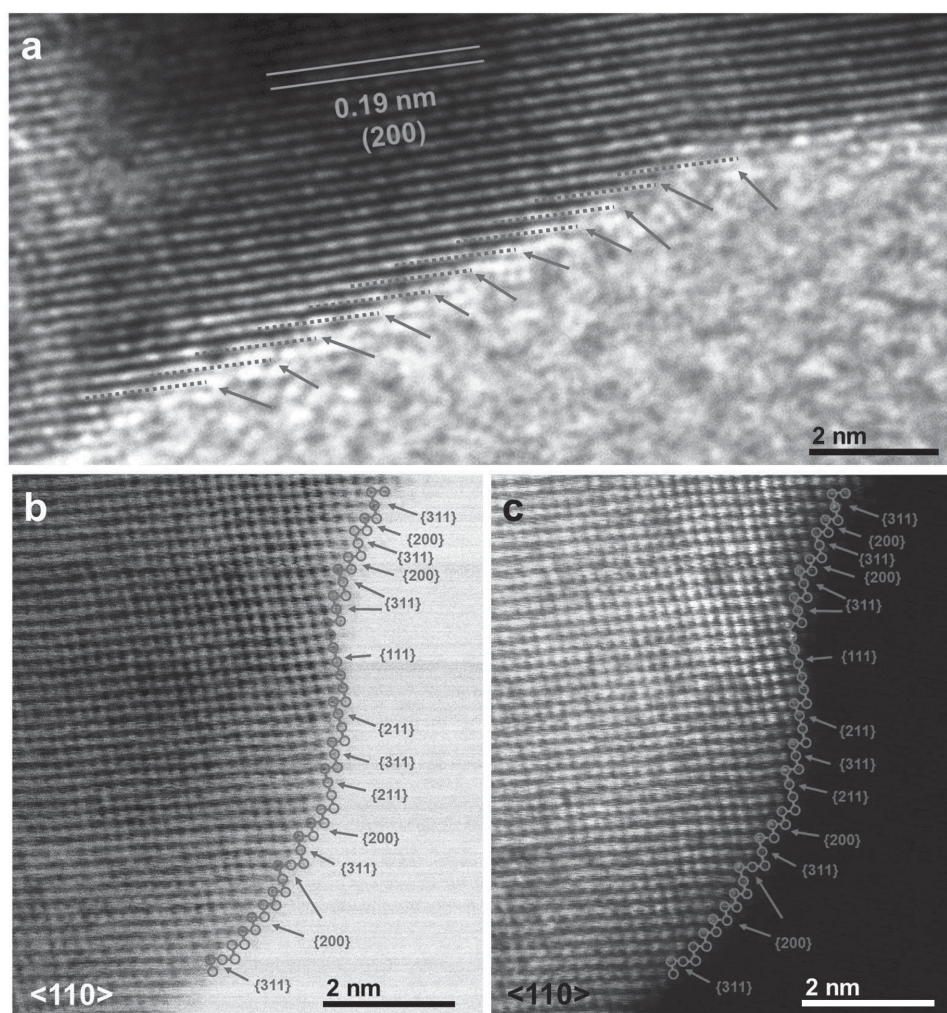


Figure 2. Structure analysis of 1D PtNi nanostructures. a) HRTEM, aberration-corrected, b) STEM BF, and c) ADF images of the 1D PtNi nanostructures, showing a large density of surface steps.

The products were 1D nanostructure mixed with branched nanocrystals when the amount of CTAC was reduced from 32 to 16 mg in the standard procedure (Figure S4c,d, Supporting Information). The structure was almost unaffected by increasing the amount of CTAC from 32.0 to 64.0 mg (Figure S4e,f, Supporting Information). The 1D PtNi nanostructures could also be obtained by replacing CTAC with cetyltrimethyl ammonium bromide (CTAB) whereas particulate nanostructures with large size were produced when CTAC was changed by NH_4Cl (Figure S5, Supporting Information). It can, therefore, be concluded that CTA^+ was the structure-directing agent and a certain amount of CTA^+ controlled the growth of 1D nanostructures in the present synthesis. (2) The production of the PtNi NWs was also affected by glucose. The product with low percent of 1D nanostructure was obtained when the reaction was carried out in the absence of glucose. The optimized results reveal that a broad range of glucose could produce 1D PtNi nanostructure (Figure S6, Supporting Information). (3) The replacement of glucose with ascorbic acid (another widely used reducing agent) in the synthesis, keeping all other synthetic conditions the same, could result in the formation of star-like nanocrystals (Figure S7, Supporting Information). Thus, the selective use of CTA^+ and the combination of glucose are responsible for the fine-controlled production of 1D PtNi

alloy nanostructures by this new method (Figures S4–S9, Supporting Information).

Although an intensive literature search for Pt alloy nanostructure syntheses achieved by the wet-chemical method shows hundreds of different synthesis protocols for Pt alloy nanostructures with different sizes, compositions, and morphologies, a general and robust approach to the production of 1D Pt alloy nanostructures remains a significant challenge.^[18–32,39–42] To understand the growth mechanism of the PtNi nanowires, we have carefully investigated their growth process and characterized the growth intermediates at different reaction times. TEM results show that ultrathin nanowires with the diameter of around 1 nm were already formed at the initial stage of the reaction (40 min). These ultrathin nanowires are of essentially pure Pt nanostructures, as revealed by the EDS and PXRD analyses (Figure 3a–c). When prolonging the reaction time to 60 min, the ultrathin nanowires evolved into thicker nanowires, with the average diameter increased to 11 nm (Figure 3a and Figure S10, Supporting Information). Surprisingly, a large portion of Ni was found in these 1D nanostructures with the composition of $\text{Pt}_{35}\text{Ni}_{65}$, implying that the reduction of $\text{Ni}(\text{acac})_2$ dominated the later growth process (Figure 3b). Interestingly, these 1D nanostructures possess two different regions that contrast clearly with one another (Figure 3d,e, and Figure S10,

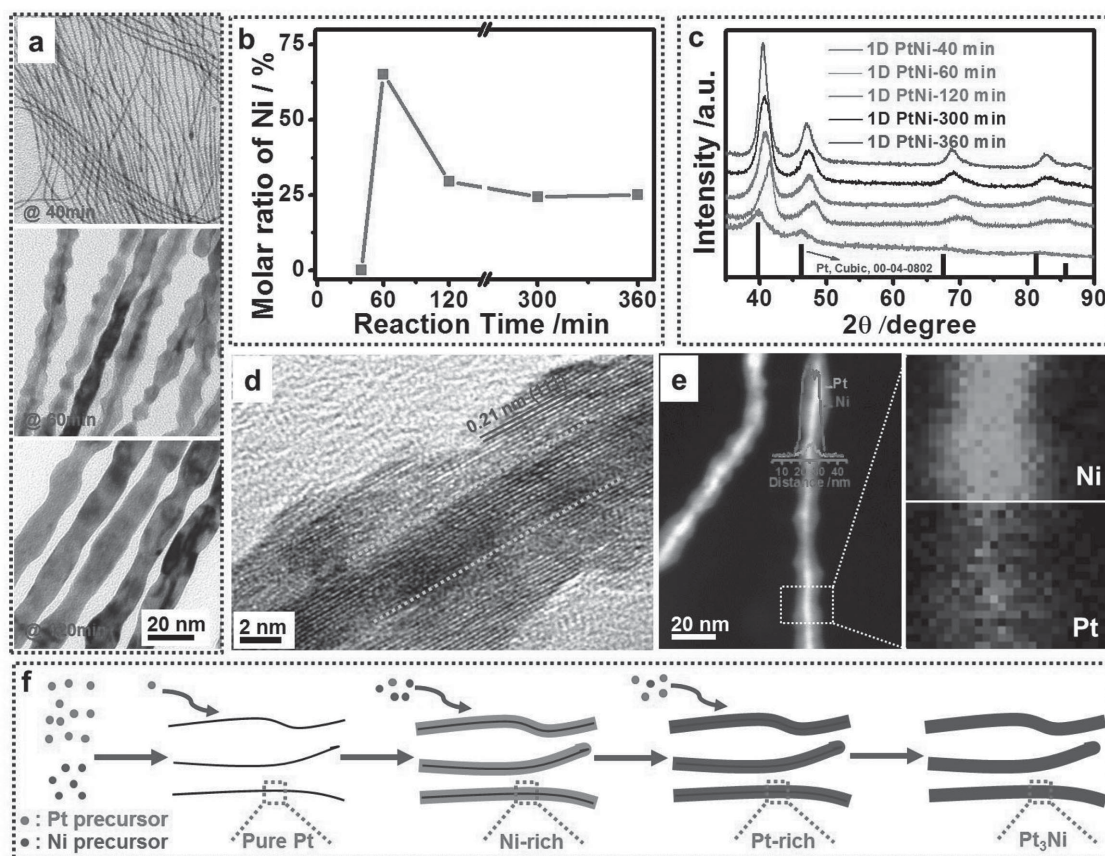


Figure 3. Growth mechanism for the unique 1D PtNi nanostructures. a) Typical TEM images of 1D PtNi intermediates collected from the reactions at different reaction times. b) The composition changes of Ni to Pt for 1D PtNi intermediates, as determined by ICP-AES measurements. c) PXRD patterns of 1D PtNi intermediates collected from the reactions at different reaction times. d) HRTEM image and e) HAADF-STEM elemental mapping of 1D PtNi intermediate collected at 60 min reaction. f) Schematic illustration of the growth mechanism of the unique 1D PtNi nanostructures.

Supporting Information), indicating the possible presence of different phases in the intermediate. The compositional line scanning profiles and elemental mapping obtained by HAADF-STEM energy dispersive X-ray spectroscopy collectively reveal that the Ni element distributes homogeneously throughout the whole area and the Pt element has higher content in the inner region (Figure 3e). In particular, these intermediates are essentially heterostructures in which PtNi₂ encircles Pt₃Ni core, as revealed by the PXRD (Figure 3c and Figure S10, Supporting Information). Together with the disappearance of the different contrast in the 1D nanostructures, a great increase in the Pt content of the intermediates (Pt₇₀Ni₃₀) was observed after a reaction time of 2.0 h (Figure 3a,b). This result implies that the reduction of Pt(acac)₂ dominated this growth process (Figure 3b). When the reaction time was 5.0 h, typical 1D nanostructures were obtained (Figure 1) with a Pt/Ni ratio of about 3:1 (Pt₇₄Ni₂₆). When the reaction time was increased to 6 h, no significant change in the structure was observed (Figure S11, Supporting Information). These time-dependent morphology and composition changes reveal that the formation of unique 1D PtNi nanostructures relied upon the initial formation of ultrathin Pt nanowires, the quick reduction of Ni species onto the preformed nanowires, and, hereafter, the diffusion of Pt into the Ni-rich 1D nanostructures (Figure 3f). The initial formation of ultrathin Pt nanowires suggests a faster reduction of Pt ions relative to Ni ions, which, in turn, is related to a more positive reduction potential of Pt ions than that of Ni ions. Thereafter, the deposition of Ni phase was accelerated, and the growth of the Pt phase was slowed down because of the largely depletion of the Pt precursor. After the depletion of both the Pt precursor and the Ni precursor, the diffusion of Pt into the Ni-rich nanowire is reasonable due to the driving force for the formation of phase table Pt–Ni alloys.

The most exciting part of our new synthesis for 1D PtNi nanostructures is quite robust, and it can be extended to the production of other 1D Pt alloy nanostructures with different compositions simply by introducing Pt(acac)₂ and desired acetylacetonates in the similar synthetic procedure. Table S1 (Supporting Information) summarizes the major synthetic parameters and resulting nanostructures. Figure 4 and Figures S12–S17 (Supporting Information) show the detailed characterizations for different types of 1D Pt alloy nanostructures, such as 1D PtCo (Figure 4b), 1D PtFe (Figure 4c), 1D PtRh (Figure 4d), and 1D PtNiFe (Figure 4e), etc. In all cases, unique 1D Pt alloy nanostructures with different compositions were obtained in high yield and high purity. According to the statistics based on the TEM observations (Figure 4, Figures S12–S17, Supporting Information, and Table S1, Supporting Information), all the 1D Pt alloy nanostructures have the lengths over 100 nm and diameters in the range of 10–20 nm. The microstructures of all these 1D Pt alloy nanostructures were thoroughly characterized by various techniques. The powder X-ray diffraction patterns show that all the 1D Pt alloy nanostructures have fcc structure that is typical for noble metals (Figures S12–S17, Supporting Information). They have highly crystalline feature, as conformed by HRTEM images (Figure 4i and Figures S12–S17, Supporting Information). The alloyed structures were confirmed by the STEM-EDS elemental mapping analysis, where the distribution of Pt and the other elements is even through the selected area

(Figure 4g,h and Figures S12–S17, Supporting Information). TEM-EDS analysis reveals the successful synthesis of Pt alloy nanostructures (Figures S12–S17, Supporting Information). ICP-AES was used to fully characterize the composition of the 1D Pt alloy. Pt_{74.2}Ni_{25.8}, Pt_{49.2}Ni_{50.8}, Pt_{76.6}Co_{23.4}, Pt_{79.6}Fe_{20.4}, Pt_{73.3}Rh_{26.7}, Pt_{58.2}Ni_{23.6}Co_{18.2}, and Pt_{60.3}Ni_{22.2}Fe_{17.5} were the final compositions (Table S1, Supporting Information).

Recent studies suggest that PtNi nanostructures are a promising class of unique electrocatalysts with high ORR activity due to the well-known electronic effect of Ni to Pt.^[16,17,20] The unique structure of the produced 1D PtNi nanostructure herein can potentially offer the new possibility for boosting ORR performance. To this end, we chose the ORR to evaluate the catalytic properties of the 1D PtNi nanostructures. Before the ORR measurements, the PtNi nanowires were loaded on a commercial carbon (C, Vulcan) support by sonicating the mixture of 1D PtNi nanostructures and C in cyclohexane, and then washed with a mixture of cyclohexane and ethanol for four times. Such treatments allowed 1D PtNi nanostructures uniformly distributed on C (1D PtNi/C, 20 wt% Pt on Vulcan XC72R carbon) (Figure S18, Supporting Information). To test its catalytic performance toward the ORR, the 1D PtNi/C was dispersed in a mixture of ethanol/water/Nafion and then casted onto a glassy carbon electrode. The commercial Pt/C from JM (Pt/C, 20 wt% Pt on Vulcan XC72R carbon) was used as a benchmark catalyst (Figure S19a,b, Supporting Information). The loading amounts of Pt were measured to be 2.0 and 2.5 μg for 1D PtNi/C and Pt/C, respectively. The insets of Figure 5a,b show the cyclic voltammograms (CVs) of these two catalysts recorded in N₂-purged 0.1 M perchloric acid solution at a sweep rate of 50 mV s⁻¹. The electrochemically active surface areas (ECSAs) of these catalysts were calculated to be 43.4 and 67.5.0 m² g⁻¹ for 1D PtNi/C and Pt/C catalysts, respectively. Figure 5a,b shows the ORR polarization curves for the different catalysts recorded at room temperature at a sweep rate of 10 mV s⁻¹. The kinetic currents were calculated from the ORR polarization curves by considering the mass-transport correction^[3] and normalizing with respect to both ECSA and the loading amount of metal Pt. As shown in Figure 5c, the 1D PtNi/C exhibits a specific activity of 9.2 mA cm⁻² at 0.9 V versus RHE with an impressive improvement factor of 51.1 over Pt/C catalyst, representing one of the highest specific activities ever achieved in ORR nanocatalysts. The mass activity of 1D PtNi/C catalyst is determined to be 4.15 A mg_{Pt}⁻¹, which is 34.6-fold higher than that of Pt/C catalyst. Both the specific and mass activities of the 1D PtNi/C are much higher than those of the state-of-the-art PtNi nanocatalysts^[20,43,44] and even comparable to those of very recently reported PtNi nanoframe catalysts (Figure 5d),^[17] making the 1D PtNi/C catalysts among the most active electrocatalysts achieved in ORR catalysts reported to date. These results further emphasize the multiple catalysis enhancements from shape, alloy, and atomic steps of 1D Pt₃Ni nanostructures.

The 1D PtNi/C catalyst also shows excellent electrochemical durability. The electrochemical durability of the 1D PtNi/C catalyst was studied by using an accelerated durability test between 0.6 and 1.1 V (vs RHE) in 0.1 M HClO₄ at a scan rate of 50 mV s⁻¹. The CVs and ORR polarization curves of the different catalysts after 10 000 potential cycles are shown in Figure 5a,b. After 10 000 potential cycles, the changes on both

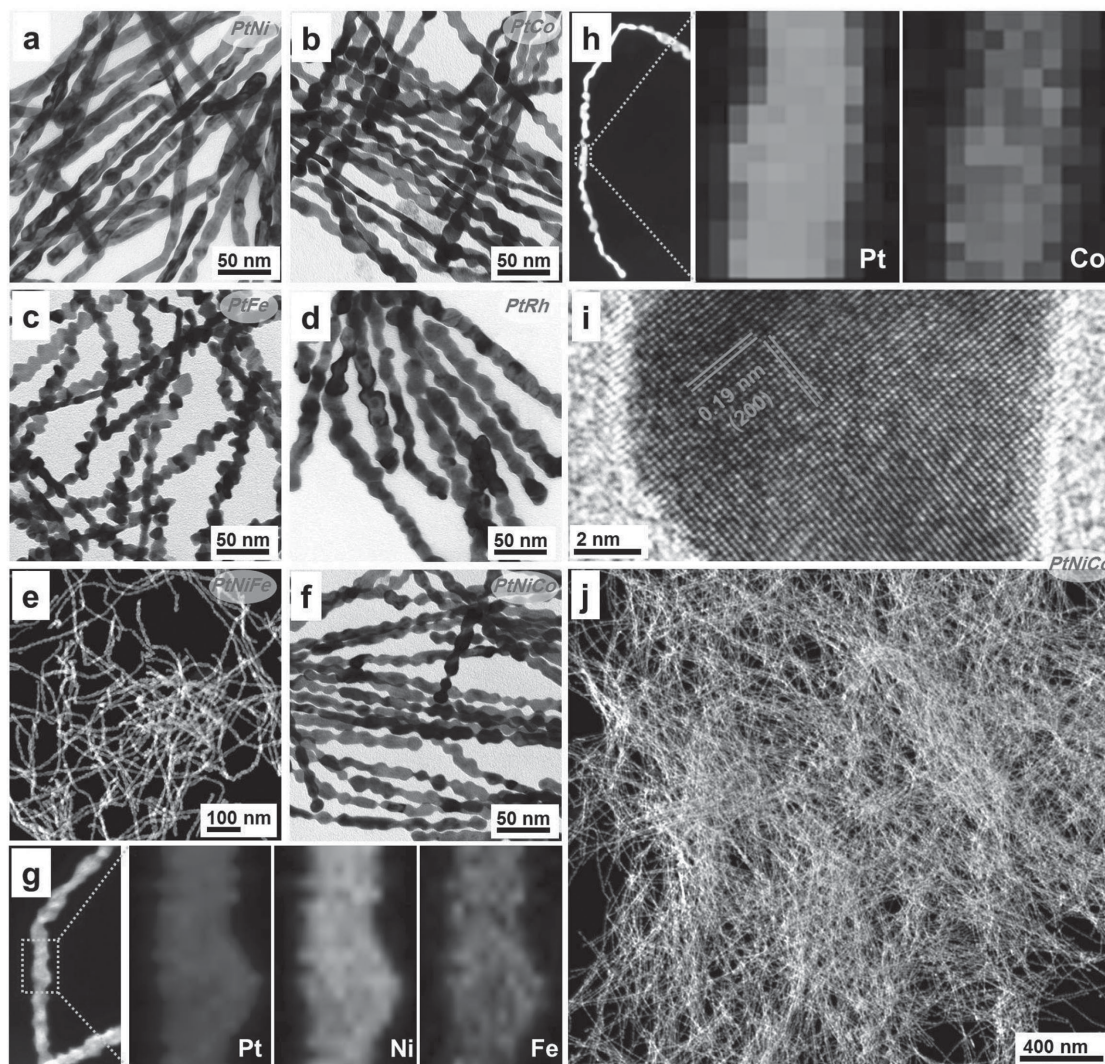


Figure 4. The production of various 1D Pt alloy nanostructures. TEM images of: a) 1D PtNi ($\text{Pt}_{49.2}\text{Ni}_{50.8}$) nanostructures, b) 1D PtCo nanostructures, c) 1D PtFe nanostructures, d) 1D PtRh nanostructures, and f) 1D PtNiCo nanostructures. STEM images of: e) 1D PtNiFe nanostructures and j) 1D PtNiCo nanostructures. HAADF-STEM elemental mappings of: g) 1D PtNiFe nanostructures and h) 1D PtCo nanostructures. i) HRTEM image of 1D PtNiCo nanostructures.

the ECSA and electrocatalytic activity of different catalysts were analyzed. As shown in Figure 5c, the specific and mass activities of the 1D PtNi/C catalyst were still as high as 8.6 mA cm^{-2} and $3.96 \text{ A mg}_{\text{Pt}}^{-1}$, which is 48-fold ($\approx 93.5\%$ of the initial value) and 33-fold (95.4% of the initial value) higher than the initial values of commercial Pt/C catalyst after 10 000 cycles. There was a small increase in ECSA for the 1D PtNi/C (from 43.4 to $47.5 \text{ m}^2 \text{ g}^{-1}$). After the stability tests, the catalysts were collected and scratched off the electrode by sonication for further TEM and STEM images characterizations. The small increase of the ECSA was likely to result from the formation of Pt-rich surface after potential cycles, as confirmed by HAADF-STEM elemental mapping (Figure 5e). In contrast, the Pt/C catalyst was unstable under the same reaction conditions, and only 58.3% of the initial ECSA, 47.5% of the mass activity, and 75.0% of the specific activity could be retained after the durability tests. After the durability tests, these catalysts were also

examined by TEM. As shown in Figure 5f and Figure S20 (Supporting Information), the morphology of 1D PtNi nanostructures was still largely maintained (Figure 5g and Figure S18, Supporting Information), but serious sintering and aggregation were observed for the Pt/C catalyst (Figure S19c,d, Supporting Information). Therefore, the combination of 1D feature of PtNi nanowires and the formation of the unique Pt-rich surface are the two major contributors to the high durability of the 1D PtNi/C sample.

Here, we carried out density functional theory (DFT) calculations to shed light on the experimental results. It has been well established that the oxygen adsorption energy (E_{O}) is an excellent descriptor for ORR activity. There exists an optimal E_{O} value under which the ORR activity of the catalyst reaches the maximum. It turns out that the optimal E_{O} is 0.2 eV higher than the E_{O} value on Pt(111) surface.^[45,46] ΔE_{O} value reported in this paper is defined relative to this optimal value. Thus,

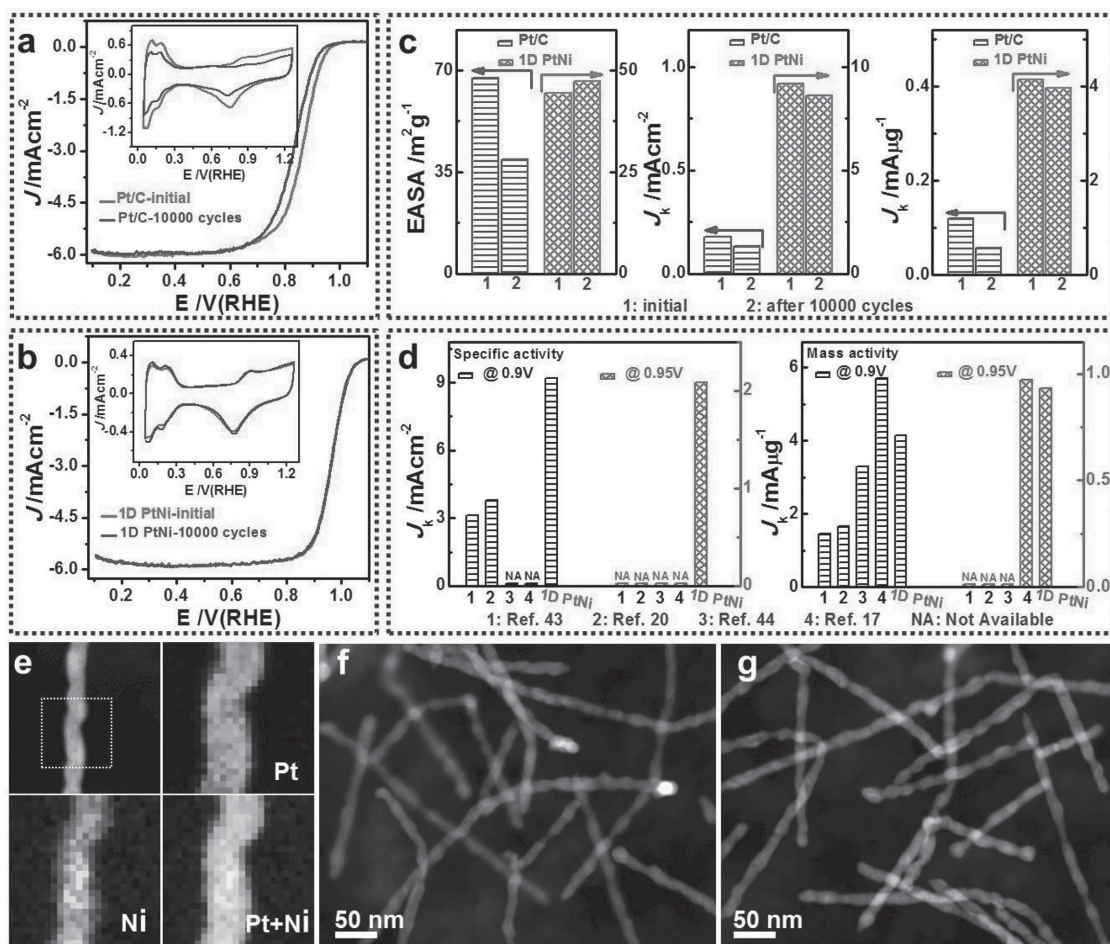


Figure 5. Electrocatalytic performance of 1D PtNi/C and commercial Pt/C catalysts. ORR polarization curves and (inset) CVs of a) the commercial Pt/C and b) 1D PtNi/C catalysts before and after 10 000 potential cycles between 0.6 and 1.1 V versus RHE. The CVs were recorded at room temperature in N_2 -purged 0.1 M $HClO_4$ solution with a sweep rate of 50 mV s^{-1} . The ORR polarization curves were recorded at room temperature in an O_2 -saturated 0.1 M $HClO_4$ aqueous solution at a sweep rate of 10 mV s^{-1} and a rotation rate of 1600 rpm. c) The changes on EASAs (left panel), specific activities (middle panel), and mass activities (right panel) of commercial Pt/C catalyst and 1D PtNi/C catalyst before and after 10 000 potential cycles. The durability tests were carried out at room temperature in O_2 -saturated 0.1 M $HClO_4$ at a scan rate of 50 mV s^{-1} . d) Comparison of specific and mass activities of 1D PtNi/C catalyst with state-of-the-art PtNi nanocatalysts. e) Elemental mapping and f) HAADF-STEM images of the 1D PtNi/C after 10 000 cycles. g) HAADF-STEM image of the 1D PtNi/C.

a catalyst with ΔE_O closer to the optimal value is believed to exhibit a superior ORR activity. Since a high density of (211) and (311) surfaces was observed in HRTEM, we focus on the two surfaces as the representatives of high-index facets on the nanowire. Furthermore, to model the dissolution of Ni atoms under the electrochemical environment, we considered the ORR activities on two systems: pure Pt surfaces and Pt_3Ni surfaces with top-layer Ni atoms completely removed. The DFT calculations show that the lattice constant of Pt_3Ni is $\approx 2.3\%$ smaller than that of Pt, and the lattice mismatch would generate a compressive strain on the nanowire surface. Hence, ΔE_O for the two surfaces was calculated under a compressive strain, ranging from 0% to 3%, and the results are shown in Figure 6a,b. Moreover, we also calculated ΔE_O on the (111) facet of Pt NPs with the particle diameter ranging from 3 to 8 nm based on the quantum mechanics–molecular mechanics method,^[47,48] and the results are shown in Figure 6c. On the (211) and (311) stepped surfaces of the nanowires, two typical

adsorption sites were examined: the bridge site at the edge of the (211) step and the hollow site on the (211) facet. On all four surfaces, oxygen bonds too strongly to the bridge sites (ΔE_O was too negative) and ΔE_O value is insensitive to the surface strain. For the hollow sites, ΔE_O is closer to the optimal energy than that of Pt NPs, thus the ORR activity on the hollow sites of the nanowires would be superior to the Pt NPs, consistent to the experimental observations. Furthermore, the presence of Ni on the sublayers reduces the binding between the oxygen and Pt top layer as indicated in Figure 6, suggesting that the Pt_3Ni nanowires should also have higher ORR activities than the pure Pt nanowires. Therefore, the improved ORR activity by incorporating Ni stems from both strain and ligand effects are due to: (1) a compressive strain is induced on the Pt surface due to the smaller atomic size of Ni, which relieves the overbinding to oxygen.^[47] (2) The ligand effect arises from charge transfer between the surface Pt and sublayer Ni which lowers the d -band center of Pt^[16] and thus weakens the binding to oxygen.

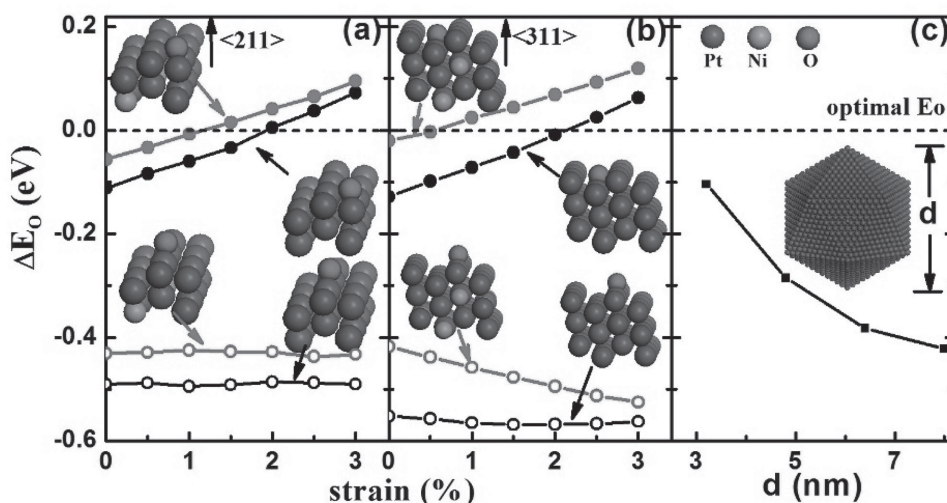


Figure 6. DFT calculations of oxygen adsorption energy. ΔE_O as a function of compressive strain on a) (211) and b) (311) surfaces. The filled circles represent ΔE_O values on the hollow sites while the open circles represent the bridge sites. The black and grey curves correspond to ΔE_O values on pure Pt and Pt₃Ni surface with top-layer Ni atoms completely removed. c) ΔE_O on the (111) facet of the Pt NPs as a function of the particle size. The NPs were modeled by icosahedra with 20 (111) facets. The horizontal dashed line indicates the optimal ΔE_O value.

In summary, we develop a general and robust approach for the production of a new class of 1D high-index faceted Pt alloy nanostructures, in which three catalysis enhancement factors are integrated (alloy effect, shape, and high index). Time-dependent TEM studies on the morphology and composition of PtNi nanostructures reveal that the formation mechanism includes three steps: (1) initial formation of ultrathin Pt nanowires, (2) the quick reduction of Ni species onto the pre-formed nanowires, and (3) the diffusion of Pt into the Ni-rich 1D nanowires. As a demonstration, we found that the unique 1D high-index faceted Pt-based multimetallic nanostructures with high density of atomic steps can deliver superior ORR specific and mass activities that are 51.1 and 34.6 times of magnitude higher than those of the state-of-the-art commercial Pt/C catalyst, respectively. Computational studies indicate oxygen adsorption energy (E_O) at the hollow site on the (211) and (311) facets is closer to the optimal E_O than that of Pt NPs, which can further enhance the ORR activity of PtNi nanowires. Significantly, the obtained 1D high-index faceted PtNi nanostructures are highly stable in the ORR condition with negligible activity decay over the course of 10 000 cycles. We believe that the achievement of large-scalable production of such high-quality 1D Pt alloy nanostructures will open up exciting opportunities toward the rational design of practically relevant catalysts with superior activity and high durability, which can significantly impact the broad areas such as batteries, fuel cells, fine chemical production, and beyond.

Supporting Information

Supporting Information is available from the Wiley Online Library or from the author.

Acknowledgements

This work was financially supported by the start-up funding from Soochow University and Young Thousand Talented Program. TEM

work carried out in part at the Center for Functional Nanomaterials, Brookhaven National Laboratory, which is supported by the U.S. Department of Energy, Office of Basic Energy Sciences, under Contract No. DE-SC0012704.

Work at California State University Northridge was supported by the Army Research Office via grant W911NF-11-1-0353.

Received: June 8, 2015

Revised: July 30, 2015

Published online: October 13, 2015

- [1] E. V. Shevchenko, D. V. Talapin, N. A. Kotov, S. O'Brien, C. B. Murray, *Nature* **2006**, 439, 55.
- [2] N. Tian, Z. Y. Zhou, S. G. Sun, Y. Ding, Z. L. Wang, *Science* **2007**, 316, 732.
- [3] B. Lim, M. J. Jiang, P. H. C. Camargo, E. C. Cho, J. Tao, X. M. Lu, Y. M. Zhu, Y. N. Xia, *Science* **2009**, 324, 1302.
- [4] Y. Tang, M. Ouyang, *Nat. Mater.* **2007**, 6, 754.
- [5] A. C. Chen, P. Holt-Hindle, *Chem. Rev.* **2010**, 110, 3767.
- [6] S. J. Guo, S. Zhang, S. H. Sun, *Angew. Chem. Int. Ed.* **2013**, 52, 8526.
- [7] J. Tollefson, *Nature* **2008**, 451, 877.
- [8] M. K. Debe, *Nature* **2012**, 486, 43.
- [9] S. E. Habas, H. Lee, V. Radmilovic, G. A. Somorjai, P. D. Yang, *Nat. Mater.* **2007**, 6, 692.
- [10] H. A. Gasteiger, N. M. Markovic, *Science* **2009**, 324, 48.
- [11] F. A. D. Bruijn, V. A. T. Dam, G. J. M. Janssen, *Fuel Cells* **2008**, 8, 3.
- [12] H. A. Gasteiger, S. S. Kocha, B. Sompalli, F. T. Wagner, *Appl. Catal. B* **2005**, 56, 9.
- [13] H. Zhang, M. Jin, Y. Xia, *Chem. Soc. Rev.* **2012**, 41, 8035.
- [14] N. S. Porter, H. Wu, Z. Quan, J. Fang, *Acc. Chem. Res.* **2013**, 46, 1867.
- [15] J. Wu, H. Yang, *Acc. Chem. Res.* **2013**, 46, 1848.
- [16] V. R. Stamenkovic, B. Fowler, B. S. Mun, G. Wang, P. N. Ross, C. A. Lucas, N. M. Markovic, *Science* **2007**, 315, 493.
- [17] C. Chen, Y. Kang, Z. Huo, Z. Zhu, W. Huang, H. L. Xin, J. D. Snyder, D. Li, J. A. Herron, M. Mavrikakis, M. Chi, K. L. More, Y. Li, N. Markovic, G. A. Somorjai, P. Yang, V. R. Stamenkovic, *Science* **2014**, 343, 1339.

- [18] D. F. van der Vliet, C. Wang, D. Tripkovic, D. Strmcnik, X. F. Zhang, M. K. Debe, R. T. Atanasoski, N. M. Markovic, V. R. Stamenkovic, *Nat. Mater.* **2012**, *11*, 1051.
- [19] D. Wang, H. L. Xin, R. Hovden, H. Wang, Y. Yu, D. A. Muller, F. J. DiSalvo, H. D. Abruña, *Nat. Mater.* **2013**, *12*, 81.
- [20] C. Cui, L. Gan, M. Heggen, S. Rudi, P. Strasser, *Nat. Mater.* **2013**, *12*, 765.
- [21] J. B. Wu, A. Gross, H. Yang, *Nano Lett.* **2011**, *11*, 798.
- [22] J. Zhang, J. Y. Fang, *J. Am. Chem. Soc.* **2009**, *131*, 18543.
- [23] Y. J. Kang, C. B. Murray, *J. Am. Chem. Soc.* **2010**, *132*, 7568.
- [24] J. Kim, Y. Lee, S. H. Sun, *J. Am. Chem. Soc.* **2010**, *132*, 4996.
- [25] D. Xu, Z. P. Liu, H. Z. Yang, Q. S. Liu, J. Zhang, J. Y. Fang, S. Z. Zou, K. Sun, *Angew. Chem. Int. Ed.* **2009**, *48*, 4217.
- [26] J. Y. Chen, B. Wiley, J. McLellan, Y. J. Xiong, Z. Y. Li, Y. N. Xia, *Nano Lett.* **2005**, *5*, 2058.
- [27] Z. M. Peng, H. Yang, *J. Am. Chem. Soc.* **2009**, *131*, 7542.
- [28] L. Wang, Y. Nemoto, Y. Yamauchi, *J. Am. Chem. Soc.* **2011**, *133*, 9674.
- [29] J. Zhang, H. Z. Yang, J. Y. Fang, S. Z. Zou, *Nano Lett.* **2010**, *10*, 638.
- [30] J. B. Wu, J. L. Zhang, Z. M. Peng, S. C. Yang, F. T. Wagner, H. Yang, *J. Am. Chem. Soc.* **2010**, *132*, 4984.
- [31] Y. E. Wu, S. F. Cai, D. S. Wang, W. He, Y. D. Li, *J. Am. Chem. Soc.* **2012**, *134*, 8975.
- [32] K. A. Kuttijiel, K. Sasaki, Y. M. Choi, D. Su, P. Liu, R. R. Adzic, *Nano Lett.* **2012**, *12*, 6266.
- [33] M. K. Carpenter, T. E. Moylan, R. S. Kukreja, M. H. Atwan, M. M. Tessema, *J. Am. Chem. Soc.* **2012**, *134*, 8535.
- [34] J. Snyder, I. McCue, K. Livi, J. Erlebacher, *J. Am. Chem. Soc.* **2012**, *134*, 8633.
- [35] S. Guo, S. Zhang, D. Su, S. Sun, *J. Am. Chem. Soc.* **2013**, *135*, 13879.
- [36] B. Y. Xia, W. T. Ng, H. B. Wu, X. Wang, X. W. Lou, *Angew. Chem. Int. Ed.* **2012**, *51*, 7213.
- [37] X. Xu, X. Zhang, H. Sun, Y. Yang, X. Dai, J. Gao, X. Li, P. Zhang, H.-H. Wang, N.-F. Yu, S. G. Sun, *Angew. Chem. Int. Ed.* **2015**, *53*, 12522.
- [38] K. Ahrenstorff, H. Heller, A. Kornowski, J. A. C. Broekaert, H. Weller, *Adv. Funct. Mater.* **2008**, *18*, 3850.
- [39] Q. Liu, Z. Yan, N. L. Henderson, J. C. Bauer, D. W. Goodman, J. D. Batteas, R. E. Schaak, *J. Am. Chem. Soc.* **2009**, *131*, 5720.
- [40] S. Guo, D. Li, H. Zhu, S. Zhang, V. R. Stamenkovic, S. Sun, *Angew. Chem. Int. Ed.* **2013**, *52*, 3465.
- [41] H. Zhu, S. Zhang, S. Guo, D. Su, S. Sun, *J. Am. Chem. Soc.* **2013**, *135*, 7130.
- [42] C. Koenigsmann, A. C. Santulli, K. Gong, M. B. Vukmirovic, W. P. Zhou, E. Sutter, S. S. Wong, R. R. Adzic, *J. Am. Chem. Soc.* **2011**, *133*, 9783.
- [43] H. Cui, L. Gan, H. H. Li, S. H. Yu, M. Heggen, P. Strasser, *Nano Lett.* **2012**, *12*, 5885.
- [44] S. I. Choi, S. F. Xie, M. H. Shao, J. H. Odell, N. Lu, H. C. Peng, L. Protsailo, S. Guerrero, J. H. Park, X. H. Xia, J. G. Wang, M. J. Kim, Y. N. Xia, *Nano Lett.* **2013**, *13*, 3420.
- [45] J. K. Norskov, J. Rossmeisl, A. Logadottir, L. Lindqvist, *J. Phys. Chem. B* **2004**, *108*, 17886.
- [46] V. Stamenkovic, B. S. Mun, K. J. J. Mayrhofer, P. N. Ross, N. M. Markovic, J. Rossmeisl, J. Greeley, J. K. Norskov, *Angew. Chem. Int. Ed.* **2006**, *45*, 2897.
- [47] X. Zhang, G. Lu, *J. Phys. Chem. Lett.* **2014**, *5*, 292.
- [48] X. Zhang, G. Lu, W. A. Curtin, *Phys. Rev. B* **2013**, *87*, 054113.